11th World Congress on Computational Mechanics (WCCM XI)
5th European Conference on Computational Mechanics (ECCM V)
6th European Conference on Computational Fluid Dynamics (ECFD VI)
E. Oñate, J. Oliver and A. Huerta (Eds)

FLOW CONTROL USING A DBD PLASMA ACTUATOR FOR HORIZONTAL-AXIS WIND TURBINE BLADES OF SIMPLE EXPERIMENTAL MODEL

Hikaru Aono[1*], Yoshiaki Abe[2], Makoto Sato[1], Aiko Yakeno[1], Koichi Okada[3], Taku Nonomura[1], and Kozo Fujii[1]

[1] Japan Aerospace Exploration Agency, 3-1-1 Yoshinodai, Chuo, Sagamihara, Kanagawa JAPAN, aono,sato,yakeno,nonomura,fujii@flab.isas.jaxa.jp
[2] The University of Tokyo, 3-1-1 Yoshinodai, Chuo, Sagamihara, Kanagawa JAPAN, abe@flab.isas.jaxa.jp
[3] Ryoyu Systems Co. Ltd., Nagoya, Aichi JAPAN, okada@flab.isas.jaxa.jp

Key words: Separated Flow Control, Large-eddy Simulation, DBD Plasma Actuator

Abstract. *Aerodynamics of horizontal axis wind turbine blades of a simple experimental model with an active flow control using a DBD plasma actuator has been studied by large-eddy simulations based on a high-order accurate and resolution computational method. Large-scale parallel computations have been conducted using message passing interfaces and 9,584 cores of the K computer. Results correspond to first revolution after the DBD plasma actuator starts have been presented. The impacts of the DBD plasma actuator on flow fields around the blades have been discussed. Up to a 14% increase in revolution-averaged torque generation has been attained. Moreover, this improvement of torque generation due to the DBD plasma actuator has been similar to those reported in the experiment.*

1 INTRODUCTION

Wind power is considered to be a part of the major sustainable energies for the next generation in the world. However, it is still a challenge to generate the stable electric power by the wind turbines. One of main reasons is that the flow around the wind turbine blades easily separates because of a change in operational conditions and environment surrounding. Thus, it is necessary to study not only blade enlarging technologies but also active flow control technologies for the wind turbines so as to realize a more efficient wind power generation system including a more stable power generation element[1, 2].

One of the active flow control devices named a non-thermal dielectric barrier discharge(DBD) plasma actuator has been known (e.g. [3, 4]). Compared with conventional devices they have the advantages of size, weight, structure, energy consumption, responsivity, and manufacturing cost.[3, 4] Figure 1 shows a schematic diagram of a single DBD

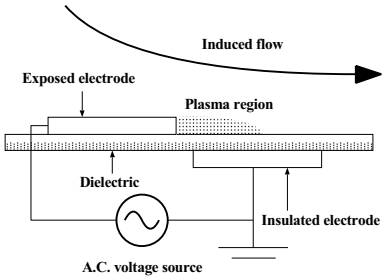

Figure 1: Configuration of asymmetric DBD actuator.

actuator that is usually composed of two thin electrodes asymmetrically flush mounted on a dielectric wall. Active control of flow separation over stationary airfoils using such DBD plasma actuators has been actively studied and an improvement in aerodynamic performance has been demonstrated. [3, 4] One of most important findings from previous studies is that when the DBD plasma actuator operates in the unsteady manner (i.e. a duty cycle or a burst modulation), the suppression of flow separation can be realized with lower power than that of with the steady actuation. Based on such useful findings obtained in previous studies, three experimental studies about the flow control using the DBD plasma actuator for the wind turbine[5, 6, 7] have been carried out. Matsuda et al.[5] have contructred a small horizontal axis wind turbine(a 1.56 meter diameter three-bladed wind turbine) and demonstrated that an improvement of the wind turbine is realized in the low velocity region in the controlled case for both yaw angle 15 and 30 degrees by wind tunnel tests. Mitsuo et al.[7] have developed a horizontal-axis wind turbine of simple experimental model (a 2.376 meter diameter three-bladed wind turbine) and shown the improvement in torque by the flow control using the DBD plasma actuator through wind tunnel experiments. More recently, Tanaka et al.[6] have conduced the first field test of plasma aerodynamic controlled 30k Watt wind turbine (a 10 meter diameter three-bladed wind turbine) and presented that the enhancement in rotor torque was confirmed when the tip speed ratio was lower than 5.5 in the case of 60 rpm in fixed rotational speed. To the best of our knowledge, aforementioned studies have not adaquetely discussed regarding flow structures including time-varying flow structures around the wind turbine blades and the influence of DBD plasma actuator on overall flow structures. Therefore, the aim of current study is to gain further understanding of fluid dynamics associated with the wind turbine blades with uncontrolled and controlled by the DBD plasma actuator.

2 Flow Conditions and Wind Turbine Model

A simple horizontal axis wind turbine model[7] is considered whereas a nacelle and a pole are not included in current simulations (see Fig. 2). A geometrical angle of attack is set to be 10 degrees with respect to the rotational plane and the blade rotates with a constant angular frequency (174 rpm). A position of the blade is represented by the

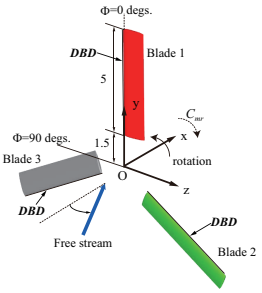

Figure 2: Configuration of a horizontal axis wind turbine blade model.

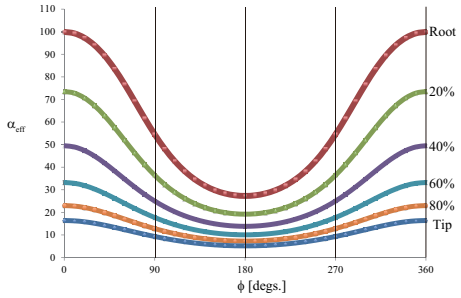

Figure 3: Time histories of effective angle of attack at selected spanwise sections.

azimuthal angle (ϕ) and ϕ=0 and 90 degrees correspond to the blade with 12 and 9 o'clock direction from the view point of upstream. A tip-speed ratio is approximately 2. A chord-and-freestream-based Reynolds number of 133,333, a non-dimensional angular frequency of 0.058, and Mach number of 0.07 is considered based on the experiment[7]. A freestream is inclined at an angle of 40 degrees with respect to the rotational axis. An aspect ratio of the blade is 5 and a cross-sectional shape is NACA0012 (see Fig. 2). It should be noted that this flow condition may or may not often occur in practice. Time variations of the effective angle of attack (α_{eff}) at selected spanwise sections are plotted in Fig. 3. The effective angle of attack decreases when the azimuthal angle changes from 0 to 180 degrees.

3 Governing Equations

Three-dimensional spatially-filtered Navier-Stokes equations, non-dimensionalized by the freestream density, freestream velocity, and the chord length of the wing, are employed as the governing equations in this study. In the non-dimensional form, the governing equations are represented as follows:

$$\frac{\partial \rho}{\partial t} + \frac{\partial \rho u_k}{\partial x_k} = 0, \tag{1}$$

$$\frac{\partial \rho u_i}{\partial t} + \frac{\partial (\rho u_i u_k + p\delta_{ik})}{\partial x_k} = \frac{1}{Re_c}\frac{\partial \tau_{ik}}{\partial x_k} + D_c S_i, \tag{2}$$

$$\frac{\partial e}{\partial t} + \frac{\partial ((e+p)u_k)}{\partial x_k} = \frac{1}{Re_c}\frac{\partial u_l \tau_{kl}}{\partial x_k} + \frac{1}{(\gamma-1)P_r Re_c M_\infty^2}\frac{\partial a^2}{\partial x_k} + D_c S_k u_k, \tag{3}$$

where x_i, u_i, q_i, ρ, p, e, τ_{ij}, S_i, δ_{ij}, γ, and t denote the non-dimensional forms of positional vector, velocity vector, heat flux vector, density, pressure, total energy per unit volume, stress tensor, body force vector, Kronecker delta, the ratio of specific heats, and time, respectively. Several non-dimensional parameters, i.e. the Reynolds(Re_c), Prandtl(P_r),

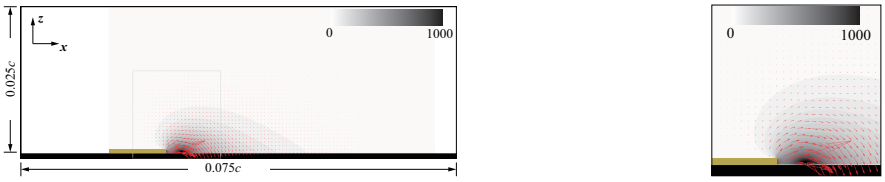

(a) overview (b) zoom-up view near the exposed electrode

Figure 4: Body force distribution of Suzen et al.'s model[9]

and Mach(M_∞) numbers, are defined as follows:

$$Re_c = \frac{\rho_\infty U_\infty c}{\mu_\infty}, P_r = \frac{\mu_\infty C_p}{\kappa_\infty}, M_\infty = \frac{U_\infty}{a_\infty}, \tag{4}$$

where μ_∞, U_∞, a_∞, C_p, and κ_∞ represent viscosity, velocity, speed of sound, constant pressure specific heat, and thermal conductivity, respectively, and the subscript ∞ denotes quantities in the freestream condition. The system is closed with the ideal gas equation of state written in the form:

$$p = (\gamma - 1)(e - \frac{1}{2}\rho u_k u_k). \tag{5}$$

Furthermore, the last terms of the right hand side in Eqs. 2 and 3 represent the momentum and the energy added to the unit volume by the body force model. Explanation of the body force model will be given in next section.

4 DBD Plasma Actuator Model

Current study models the effects of the DBD actuator on external flows as body force distribution. Several body force models[3, 8, 9] have been proposed. We have selected a simple body force model developed by Suzen et al.[9].

4.1 Spatial Distribution

Figure 4 shows contour of magnitude of non-dimensional body force and body force vectors. The dimension of the model region is $0.075c$ (chord direction) $\times$ $0.025c$ (vertical to the chord direction). The body force vector in the spanwise component is assumed to be zero because we consider an uniform geometry of DBD plasma actuator in spanwise direction. The body force model rotates 90 degrees counterclockwise about the span-axis and then is installed on the airfoil surface at 0% of the chord length from the leading edge.

4.2 Model Parameters for DBD Plasma Actuator Model

The body force is modeled with $D_c S_i$ and $D_c S_i u_k$ in the Navier-Stokes equations was stated in previous subsection. Here, the non-dimensional DBD actuator parameter (D_c)

is defined as

$$D_c = \frac{Q_{c,ref} E_{ref} c}{\rho_\infty U_\infty^2}, \tag{6}$$

where Q_c and E_i denote the electric charge and the electric-field vector, and the subscript *ref* denotes the reference value. We set $Q_{c,ref}$ and E_{ref} as the maximum values of Q_c and E in the simulation results of the model.[9] We conducted an a priori test to obtain the influence of D_c on the maximum time-averaged induced wall-parallel jet in the static air. A case with D_c of 0.5, a burst ratio ($BR = T_{on}/T^+$) of 10%, and F^+ of 1 corresponds to maximum time-averaged induced wall-parallel velocity is approximately 0.25 times to the freesteam velocity.

For time variation of the body force in Eq.2, the burst modulation[3] is considered (see Fig. 5) and a mathematical expression is given as follows:

$$D_c S_i(t) = \{ \begin{array}{ll} D_c S_{suzen}(x,y,z)\sin^2(2\pi F_{base} t) & 0 < t \leqq T_{on} \\ 0 & T_{on} < t \leqq T^+ (= 1/F^+) \end{array} \tag{7}$$

where F_{base}, T_{on}, and T^+ denote the non-dimensional base frequency($f_{base}c/U_\infty$) for the alternating current (AC) of the input voltage, the duration of the actuation is on, the period of burst actuation. Here, f_{base} is the base frequency for the AC of the input voltage. Base frequency(F_{base}) set to be 100, which is higher than that of flow fluctuation. The non-dimensional burst frequency (F^+) and the burst ratio(BR) are given then the burst wave form is generated. As stated in Eq.7 the DBD actuator fluctuation is modeled using a square of sinusoidal function because the time-varying force generated by the DBD actuator is termed as a push-push type in one cycle which is similar to the square of sinusoidal function, and not push-pull type which is similar to the sinusoidal function[10].

5 Computational Cases

One computation without the DBD plasma actuator and two computations with the DBD plasma actuator are conducted. Computational cases are listed in Table 1. Note that all parameters of controlled cases including the burst frequency and burst ratio have been determined based on previous experimental conditions[7].

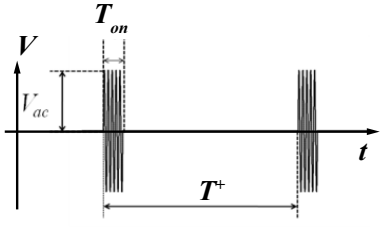

Figure 5: Schematic diagram of burst wave input signal.

Table 1: Summary of computational cases.

Case name	F^+	D_c	BR	F_{base}
OFF (uncontrolled)	-	-	-	-
F^+=1,D_c=0.5	1	0.5	0.1	100
F^+=6,D_c=0.5	6	0.5	0.1	100

6 Computational Approach

6.1 Numerical Method

An in-house fluid analysis solver, called LANS3D, is employed for all large-eddy simulations in this study. Three-dimensional compressible spatially-filtered Navier-Stokes equations are employed as the governing equations. These equations are solved in the generalized curvilinear coordinates (ξ, η, ζ). As the velocity induced by the body force is small and unsteady, a high-resolution unsteady computational method is required. The spatial derivatives of the convective and viscous terms and symmetric conservative metrics[11, 12, 13] and Jacobian[11, 12, 13] are evaluated by a sixth-order compact difference scheme.[14] Near the boundary, second-order explicit difference schemes are used. Tenth-order filtering[14, 15] is used with a filtering coefficient of 0.4. For time integration, lower-upper symmetric alternating direction implicit and symmetric Gauss-Seidel[16] methods are used. To ensure time accuracy, a backward second-order difference formula is used for time integration, and three sub-iterations[17] are adopted. The computational time step is $1.4 \times 10^{-4} c/U_\infty$ that corresponds to maximum Courant-Friedrichs-Lewy number of approximately 20. At the outflow boundary, all variables are extrapolated from one point in front of the outflow boundary. At the inflow boundary, the freestream velocity is assigned. For the airfoil surface, no-slip and adiabatic-wall conditions are adopted. For rotation of the blades all grids are rigidly rotated about the original of the coordinate as shown in Fig. 2. Coherent structure model[18] is used as the sub-grid scale model. Parallel computation has been performed using message passing interfaces. All computations have been conducted using 1198 nodes of the K computer which is based on a distributed memory architecture with over 80,000 nodes[19]. Note that compact difference scheme-related subroutines in LANS3D have been well tuned for the K computer[20].

6.2 Computational Grids

Current study employes the overset grid technique[21] to deal with the region of small body force (see Fig. 4) and multiple turbine blades. As shown in Figure 6, the grid system requires four overset grids per blade to define the blade surface and the DBD plasma actuator. These grids consist of a main blade grid, blade-tip, and blade-root and the body force region. The body force distribution is calculated on the grid corresponding to the body force model region and then the body force is mapped to the zone 6, 10, and

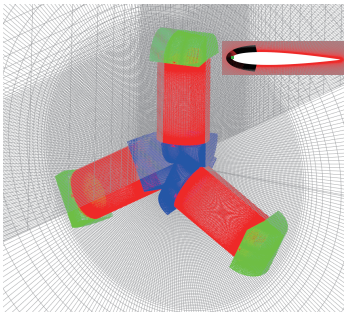

Figure 6: Perspective view of computational grids around the current wind turbine model.

Table 2: Number of computational grid point.

Name of grid	ξ	η	ζ	Total grid points
Zone 1 (Background)	337	495	1023	170,651,745
Zone 2 (Background)	41	495	41	832,095
Zone 3 (main blade 1)	201	541	101	10,982,841
Zone 4 (blade-tip 1)	188	301	101	5,715,388
Zone 5 (blade-root 1)	188	301	101	5,715,388
Zone 6 (actuator of blade 1)	319	501	81	12,945,339
Zone 7 (main blade 2)	201	541	101	10,982,841
Zone 8 (blade-tip 2)	188	301	101	5,715,388
Zone 9 (blade-root 2)	188	301	101	5,715,388
Zone 10 (actuator of blade 2)	319	501	81	12,945,339
Zone 11 (main blade 3)	201	541	101	10,982,841
Zone 12 (blade-tip 3)	188	301	101	5,715,388
Zone 13 (blade-root 3)	188	301	101	5,715,388
Zone 14 (actuator of blade 3)	319	501	81	12,945,339

14 grid beforehand. To complete the overset grid system, two background grids surround the blade volume grids. The length of outer boundary from the center of rotation is 50 of the chord. Number of grid points of each zone is tabulated in Table 2. Total number of grid points is approximately two hundred fifty million. The minimum grid size in the direction normal to the airfoil surface is 0.000274 of the chord that al least ten grid points are within the laminar boundary layer near the leading-edge.

7 RESULTS AND DISCUSSIONS

Figure 7 shows a comparison of time history of torque acting on the blade 1 for uncontrolled and controlled cases(F^+=1 and 6). The DBD plasma actuator is switched on from

second revolution of the blade 1(i.e. from $\phi = 360$ degrees shown in Fig. 7). The period of burst modulation of DBD plasma actuator is approximately ϕ of 21 degrees and DBD plasma actuator is switched on during either 2 degrees or 0.33 degrees per 21 degrees. It is found that the DBD plasma actuator enhances the torque generation during the blade revolution. Regardless of first blade revolution with the actuation of the DBD plasma actuator this improvement is of worth to possibly lead the positive feedback in the torque generation per blade revolution that has been observed in the previous study[5].

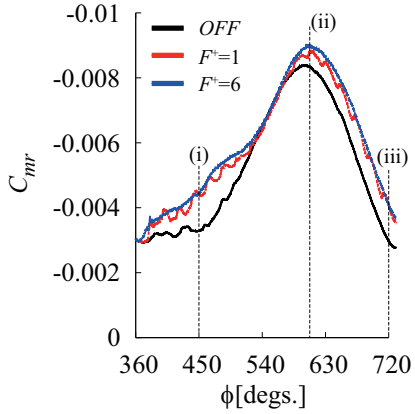

Figure 7: Time histories of torque generated by the blade 1. Black, red, and blue lines correspond to the uncontrolled case and the controlled cases with F^+=1 and 6.

During the azimuthal angle of the blade changes from 360 to 540 degrees, the effective angle of attack of the blade reduces (see Fig. 3). When the blade reaches near ϕ of 540 degrees, the improvement becomes small. At this time the effective angle of the blade is minimum. Therefore, this is expected to be the flow around the blade less separates compared to other the azimuthal angle of the blade. During ϕ changes from 540 to 720 degrees, the effective angle of attack of the blade increases (see Fig. 3). Unlike the time variation of torque during the first half revolution of the blade, almost constant improvement in the torque generation can be seen. Next instantaneous surface pressure distributions at three time instants (marked in Fig. 7) will be highlighted.

Instantaneous surface pressure distributions at ϕ of 450, 608, and 720 degrees are shown in Figs. 8, 9, and 10. Note that the pressure coefficient is normalized by the dynamic pressure of freestream. As seen in Fig. 8, all three cases present the low pressure region near the leading-edge of the blade-tip and the blade-root. It is shown that the low pressure region near the leading-edge associated with the controlled cases(F^+=1 and 6) is widen compare to that of the uncontrolled case. Looking at a comparison of surface pressure distributions at 75% of the span length, suction peaks near the leading-edge of the controlled cases is higher than that of the uncontrolled case. At a comparison of surface pressure distributions at a 50% of the span length, the suction peaks near the leading-edge of the controlled cases is slightly higher than that of the uncontrolled case. Fluctuation of the surface pressure distribution is presented due to the actuation of the

DBD plasm actuator. At 25% of the span length the suction peaks are comparable, however, the fluctuation of surface pressure is more visible in comparison with that of the uncontrolled case. This is related to the signature of vortex shedding and convection near the surfaces. Recalling time histories of torque, the difference in surface pressure distributions leads to the improvement in torque generation at this azimuthal angle.

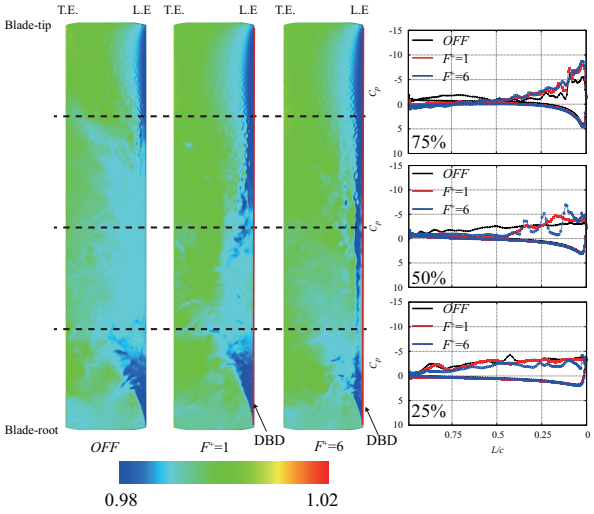

Figure 8: Instantaneous pressure distributions on the suction surface of blade 1 (left) and on selected spanwise locations (right) at the azimuthal angle of 450 degrees. Red line indicates the exposition of the DBD plasma actuator. L.E. and T.E. denote the leading-and trailing-edge.

As seen in Fig. 9, it is clear that all cases show the low pressure region near the leading-edge and the blade-tip. It is shown that the low pressure region near the leading-edge associated with the controlled cases(F^+=1 and 6) is widen compare to that of the uncontrolled case as similar to those seen in Fig. 8. Looking at a comparison of surface pressure distributions at 75% of the span length, suction peaks near the leading-edge of the controlled cases are similar to that of the uncontrolled case. Looking at surface pressure distributions at 50% of the span length, the suction peaks near the leading-edge of the controlled cases is slightly higher than that of the uncontrolled case and higher pressure peaks are observed in the controlled cases. At those at 25% of the span length the suction peaks of the controlled cases are higher than that of the uncontrolled case and the fluctuation of pressure is more visible in comparison with that of the uncontrolled case.

As seen in Fig.10, the controlled cases show low pressure region near the leading-edge of the blade-tip. At this time, the uncontrolled case becomes almost fully separated condition over the blade. While the cases with the DBD plasma actuator, at 75% of the span length the suction peak near the leading-edge is higher than that of the uncontrolled case. At 25% and 50% of the span length all cases seem to be completely separated flow.

Lastly, increases of the revolution-averaged torque for first revolution ranges between 11% and 14% by the DBD plasma actuator flow control. This improvement in torque gen-

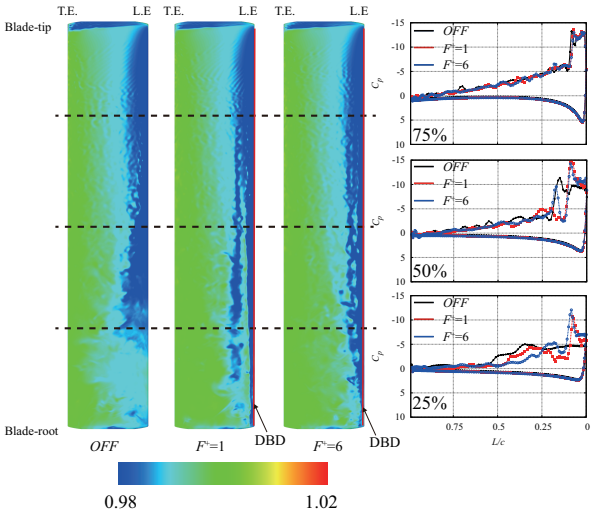

Figure 9: Instantaneous pressure distributions on the suction surface of blade 1(left) and on selected spanwise locations(right) at the azimuthal angle of 608 degrees. Red line indicates the exposition of the DBD plasma actuator. L.E. and T.E. denote the leading-and trailing-edge.

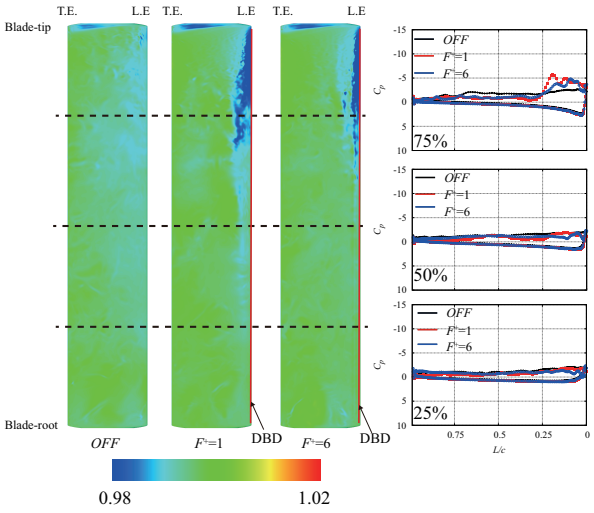

Figure 10: Instantaneous pressure distributions on the suction surface of blade 1 (left) and on selected spanwise locations (right) at the azimuthal angle of 720 degrees. Red line indicates the exposition of the DBD plasma actuator. L.E. and T.E. denote the leading-and trailing-edge.

eration due to the DBD plasma actuator is similar to those reported in the experiment[7].

8 CONCLUSIONS

Aerodynamics of simple experimental wind turbine blade model with the DBD plasma actuator flow control has been investigated by large-eddy simulations. Large-scale parallel computations have been performed using message passing interfaces and 9,584 cores of the K computer. The results for first revolution after the DBD plasma actuator switches on have been discussed. Approximately 11%-14% increase in revolution-averaged torque can be realized by the flow control using the DBD plasma actuator for the first revolution after the DBD plasma actuator switches on. The DBD plasma actuator affects the separated leading-edge shear layer and leads to delay of the leading-edge separation of wind turbine blades.

Acknowledgments

This research used computational resources of the K computer and other computers of the HPCI system provided by the AICS and the Information Technology Center, The University of Tokyo through the HPCI System Research Project (Project ID:hp130001).

REFERENCES

[1] Johnson, S.J., "Case" van Dam, C.P., Berg. D.E. Active load control technologies for wind turbines. SAND2008-4809.

[2] Barlas, T.K., van Kuik, G.A.M. Review of state of the art in smart rotor control research for wind turbines. *Prog. Aeros. Sci.* (2010) **46**: 1-27.

[3] Corke, T.C., Post, M.L. Overview of plasma flow control: concepts, optimization and applications. *AIAA 2005-563*, 2005.

[4] Moreau, E. Airflow control by non-thermal plasma actuators. *J. Phys D: Appl. Phys.* (2007) **40**: 605-636.

[5] Matsuda, H., Tanaka, M., Goshima, S., Amemori, K., Nomura, M., Osako, T. Experimental study on plasma aerodynamic control for improving wind turbine performance. AGGT2012-1058.

[6] Tanaka, M., Amemori, K., Matsuda, H., Shimura, N., Yasui, H., Osako, T., Kamada, Y., Maeda, T. Field test of plasma aerodynamic controlled wind turbine. EWEA2013-585.

[7] Mitsuo, K., Watanabe, S., Atobe, T., Ito, T., Shiohara, T., Tanaka, M. Aerodynamic characteristics improvement of a wind turbine by plasma actuators, *Proceedings of JSME* S052023 (in Japanese).

[8] Shyy, W., Jayaraman, B., Andersson, B. Modeling of glow discharged-induced fluid dynamics. *J. Appl. Phys.* (2002) **92**: 6434.

[9] Suzen, Y.B., Huang, P.G., Jacob, J.D., Ashpis, D.E. Numerical simulations of plasma based flow control application. *AIAA 2005-4633*, 2005.

[10] Font, G.I., Enloe, C.L., McLaighlin, T.E. Plasma volumetric effects on the force production of a plasma actuator. *AIAA J.* (2010) **48**: 1869-1874.

[11] Vinokur, M., Yee, H.C. Extension of efficient low dissipation high-order schemes for 3D curvilinear moving grids. *Frontiers of Computational Fluid Dynamics* (2002) 129-164.

[12] Deng, X., Min, Y., Mao, M., Liu, H., Tu, G., Zhang, H. Further studies on geometric conservation law and applications to high-order finite difference schemes with stationary grids. *J. Comp. Phys.* (2013) **239**: 90-111.

[13] Abe, Y., Nonomura, T., Iizuka, N., Fujii, K. Geometric interpretations and spatial symmetry property of metrics in the conservative form for high-order finite-difference schemes on moving and deforming grids. *J. Comp. Phys.* (2014) **260**: 163-203.

[14] Lele, S.K. Compact finite difference scheme with spectral-like resolution. *J. Comp. Phys.* (1992) **103**: 16-22.

[15] Gaitonde, D.V., Visbal, M.R. Pade type higher-order boundary filters for Navier-Stokes equations. *AIAA J.* (2000) **38**: 2103-2122.

[16] Iizuka, N. Study of mach number effect on the dynamic stability of a blunt re-entry capsule. *Ph.D Thesis*, University of Tokyo, 2006.

[17] Chakravarthy, S.R. Relaxation methods for unfactored implicit upwind schemes. *AIAA 1984-0165*, 1984.

[18] Kobayashi, H, Ham, F., Wu, X. Application of a local SGS model based on coherent structures to complex geometries. *Int. J. Heat Fluid Fl.* (2008) **29**: 640-653.

[19] Miyazaki, H., Kusano, Y., Okano, H., Nakada, T., Seki, K., Shimizu, T., Shinjo, N., Shoji, F., Uno, A., Kurokawa, M. K computer: 8.162 PetaFLOPS massively parallel scalar supercomputer built with over 548,000 cores. Solid-State Circuits Conference Digest of Technical Papers (ISSCC), 2012 IEEE International (2012) 192-194.

[20] Aono, H., Nonomura, T., Iizuka, N., Ohsako, T., Inari, T., Hashimoto, Y., Takaki, R., Fujii, K. Scalar tuning of a fluid solver using compact scheme for a supercomputer with a distributed memory architecture. *CFD letters* (2013) **5**: 143-152.

[21] Fujii, K. Unified zonal method based on the fortified solution algorithm. *J. Comp. Phys.* (1995) **118**: 92-108.